ADVANCED FUNCTIONAL MATERIALS
www.afm-journal.de

Mechanistic Insights of Zn-Ion Storage in Synergistic Vanadium-Based Composites

Lingli Xing, Xinyu Zhang, Nuo Xu, Ping Hu, Kun Wang,* and Qinyou An**

A novel composite material $Na_2V_6O_{16}\cdot 3H_2O$-$Al_xV_2O_5$ (NVO-AVO) is designed and synthesized for the first time in aqueous zinc ion battery cathode. The electrochemical behavior is elucidated in detail using in situ and ex situ techniques. The NVO-AVO is simple, inexpensive, and safe to fabricate and contributes to the synergistic effect of orthorhombic $Al_xV_2O_5$ (AVO) and monoclinic $Na_2V_6O_{16}\cdot 3H_2O$ (NVO), the NVO-AVO composites have fast Zn^{2+} kinetics and exhibit good electrochemical properties. At 300 mA g^{-1}, the specific capacity is as high as 392.5 mA h g^{-1}, and even more excitingly, NVO-AVO remains a specific capacity of 160.6 mA h g^{-1} even after 18 300 cycles at 5000 mA g^{-1}, which is significantly better than the stability of both NVO and AVO. The distinctive V_3O_8 layered structure in $Na_2V_6O_{16}\cdot 3H_2O$ facilitates the diffusion of Zn^{2+}, and structural water located between the V_3O_8 layers facilitates rapid charge transfer by widening the gallery spacing and supposing more storage sites for Zn^{2+}. In addition, $Al_xV_2O_5$ forms [AlO_6] octahedral units that enhance structural stability and play a crucial role in maintaining long-term cycling stability. This work supports the theoretical basis and technical support for the development and extension studies of new vanadium-based electrode materials.

1. Introduction

Considering the increasing cost of limited lithium resources and the safety issues arising from the inherent chemical activity of lithium metal and its flammable ester electrolyte, aqueous batteries have recently been considered promising alternatives, particularly for large-scale energy storage stations.[1–6] Of all the various aqueous batteries, aqueous zinc ion batteries (AZIBs) are receiving increasing attention due to the unique advantages of zinc's high theoretical capacity (820 mA h g^{-1}), low electrode potential (−0.76 V versus standard hydrogen electrodes), good stability in water, simple manufacturing process and nontoxicity.[7–16] However, the development of AZIBs is hampered by the slow kinetics of the divalent charge Zn^{2+} in the cathode material due to solid electrostatic interactions and suboptimal cycle life.[17] Therefore, developing a new cathode material with a stable structure, superior capacity, and high energy density would be an attractive research direction.

Current research into AZIBs cathode materials has focused on manganese-based materials, vanadium-based compounds, and Prussian blue analogs.[12,18] Manganese oxides show high operating voltages up to ≈1.3 V, but the batteries experience capacity loss during cycling due to structural breakdown.[19] Due to their high voltage, Prussian blue analogs are another attractive active material family, however, their unsatisfactory capacity (typically ≤100 mA h g^{-1}) and poor cycle life prevent their further application.[20] Vanadium-based materials typically possess high capacity and excellent rate performance due to the open-framework crystal structure and multiple oxidation states of vanadium.[21] Despite significant efforts by AZIBs, the rational design of vanadium-based materials is still in its early stages and further research is needed to improve every aspect of their property.

The most stable component of the vanadium oxide system is V_2O_5 and the quest for improved performance is ongoing.[22–25] Although V_2O_5 has a series of advantages,[26] the V_2O_5 cathode is plagued by poor cyclic stability, low ionic and electronic conductivity, and slow Zn^{2+} diffusion.[27] Recent studies indicate that the layered V_2O_5 host structure is compositionally flexible, allowing the interlayer space to accommodate pre-inserted layers of guest species, from metal ions to water as "pillars."[28–32] $Na_2V_6O_{16}\cdot 3H_2O$ is a promising cathode consisting of a V_3O_8 layer and Na^+, where the V_3O_8 layers are alternately arranged with VO_5 pentahedrons and VO_6, and more importantly, the interlayer distance is sufficient for Zn^{2+} insertion/extraction and

L. Xing, X. Zhang, N. Xu, Q. An
State Key Laboratory of Advanced Technology for Materials Synthesis and Processing
Wuhan University of Technology
Wuhan 430070, P. R. China
E-mail: anqinyou86@whut.edu.cn
P. Hu, Q. An
Hubei Longzhong Laboratory
Wuhan University of Technology (Xiangyang Demonstration Zone)
Xiangyang 441000, P. R. China
E-mail: huping316@hubu.edu.cn
K. Wang
State Key Laboratory of Silicate Materials for Architectures
Wuhan University of Technology
Wuhan 430070, P. R. China
E-mail: kun.wang@whut.edu.cn
P. Hu
School of Microelectronics
Hubei University
Wuhan 430062, P. R. China

The ORCID identification number(s) for the author(s) of this article can be found under https://doi.org/10.1002/adfm.202312773

DOI: 10.1002/adfm.202312773

H^+ can be stably present between the V_3O_8 layers.[33] Based on previous studies, we found that the capacity of $Na_2V_6O_{16}\cdot 3H_2O$ (hereinafter referred to as NVO) is high, but the cycling performance is not particularly satisfactory.[33,34] To accelerate the commercialization of large-scale energy storage systems, it is useful to enhance the electrochemical property of NVO cathodes further. Considering that trivalent Al^{3+} forms stable Al—O bonds between O atoms with a lattice energy of 15 111 kJ mol^{-1}, which is remarkably higher than that of Na—O (2478 kJ mol^{-1}).[10] Unlike the transition metal ions, the empty d orbitals and stable value state of Al 3p diminish Coulombic interactions with guest ions during cycling. Moreover, the structural model of $Al_xV_2O_5$ (hereinafter referred to as AVO) has Al^{3+} occupying part of the interlayer positions between the VO_5 plates, forming (AlO_6) octahedral units, enhancing structural stability, and facilitating the insertion and extraction of Zn^{2+}.[35] Therefore, we have attempted to design and synthesize for the first time a new composite material $Na_2V_6O_{16}\cdot 3H_2O$-$Al_xV_2O_5$ (hereinafter referred to as NVO-AVO) with enhanced synergistic effects on the AZIBs cathode. To our knowledge, NVO-AVO with a unique structure has not been reported, which requires a systematic study and in-depth investigation of the storage mechanism of Zn^{2+} in NVO-AVO composites.

Benefiting from the dual effect of the metal ion intercalation and the intrinsically conducting framework, the diffusion kinetics of Zn^{2+} and the structural stability of the hydrated vanadate are effectively improved. The NVO-AVO cathode offers a high reversible specific capacity of 392.5 mA h g^{-1} at 300 mA g^{-1}, excellent rate capability, and retains a discharge capacity of 160.6 mA h g^{-1} at 5000 mA g^{-1} for more than 18300 cycles. It was demonstrated that the compounding of the monoclinic $Na_2V_6O_{16}\cdot 3H_2O$ with orthorhombic $Al_xV_2O_5$ significantly improved the material's electrical conductivity, thus improving the battery's performance. Here, we have elucidated for the first time the reversible storage mechanism of NVO-AVO in AZIBs by in situ X-ray diffraction, in situ Raman, in situ Fourier transform infrared, in situ electrochemical impedance spectroscopy, a series of ex situ techniques, and various electrochemical analyses. We reveal a facile and elegant method to enhance the rate, capacity, and cycling stability of V_2O_5, which possesses great potential for applications of energy storage and conversion. This study is therefore of great scientific and technical importance to explore novel electrodes with significant capacitance and impressive cycling stability for AZIBs.

2. Results and Discussion

The new facile hydrothermal method was used to synthesize samples of NVO without aluminum, AVO without sodium, and composite material NVO-AVO with both aluminum and sodium sources (refer to the "Synthesis" section of the Experimental section for details). X-ray diffraction (XRD) patterns of AVO and NVO (**Figure 1a**) can be well-indexed to orthorhombic V_2O_5 (Lattice parameters: a = 11.52 Å, b = 3.57 Å, c = 4.37 Å, $\alpha = \beta = \gamma$ = 90.00, JCPDS: 00-041-1426) and monoclinic $Na_2V_6O_{16}\cdot 3H_2O$ (Lattice parameters: a = 12.17 Å, b = 3.60 Å, c = 7.78 Å, $\alpha = \gamma$ = 90.00, β = 95.03, JCPDS: 00-016-0601), respectively. In addition, the XRD peaks of NVO-AVO are the sum of all the peaks of NVO and AVO, without any extra peaks, indicating the successful combination of NVO-AVO.

In the Raman spectra, NVO-AVO shows similar morphology to AVO and belongs to the characteristic peak of V_2O_5 (Figure 1b).[10] Raman spectra in Figure 1b show the stretching and bending vibrations of chemical bonds. The Raman spectrum of NVO-AVO exhibits eight main peaks at 146, 286, 305, 408, 482, 529, 703, and 996 cm^{-1}, which can be well-attributed towards signature Raman activity vibrational modes of different vanadium/oxygen bonds.[36] Peak located at 139 cm^{-1} in the Raman spectrum of NVO assigned to bending vibration of the —V—O—V—O— chain, which is shifted to 145 and 146 cm^{-1} in the Raman spectra of AVO and NVO-AVO with stronger intensity relatively, indicating that the interaction between two neighboring V—O—V monolayers is enhanced.[37] Two Raman bands at 286 and 408 cm^{-1} correspond with the bending vibration of the V═O (I) bond, whereas peaks at 305 and 482 cm^{-1} are assigned to the bending vibrations of V—O (IV) and V—O (II) bonds. The peak at 529 cm^{-1} is the stretching vibration of the V—O (IV) bond, and at 703 and 996 cm^{-1} corresponds to the stretching modes of V—O (III) and V═O (I) bonds.[38]

In addition, Fourier transform infrared spectroscopy (FTIR) was used as a complementary characterization to Raman spectroscopy. The FTIR spectrum of NVO-AVO (Figure S1, Supporting Information), with the stretching vibration of the V—O—V bond at 773 cm^{-1} and that of the V═O bond at 998 cm^{-1}.[37] Meanwhile, the stretching and bending vibrations of O—H from structural water occur at 3443 and 1616 cm^{-1}.[22] The FTIR spectrum of NVO contains O—H, while the FTIR spectrum of AVO has disappeared. The thermal stability of these samples was examined by thermogravimetric analysis (TGA) (Figure S2, Supporting Information), the AVO showed no significant weight loss and exhibited good thermal stability. The TGA curve for NVO-AVO shows two dehydration steps with the first stage of weight loss corresponding to the removal of slightly adsorbed structural water. The second stage of dehydration is the removal of the residual compactly bound lattice water. Meanwhile, the TGA curves confirm that the crystal water in NVO mainly causes the difference in total weight loss between NVO and AVO. These water molecules between the NVO layers acting as a "lubricant" benefit the electrochemical insertion/extraction of divalent Zn^{2+}.

The Bruno–Emmett–Teller (BET) surface area analysis (Figure S3, Supporting Information) gives specific surface areas of NVO, AVO, and NVO-AVO are 24.08, 2.05, and 9.41 m^2 g^{-1}. Further, X-ray photoelectron spectroscopy (XPS) was used to collect the elemental composition and electronic states. The survey XPS spectrum confirmed the presence of Na, Al, V, and O elements in NVO-AVO (Figure S4, Supporting Information). A significant Na signal was present in both NVO and NVO-AVO samples, while no Na signal was observed in AVO, and the high-resolution Na 1s spectrum of the NVO-AVO sample is shown in Figure 1c. In addition, the high-resolution Al 2p spectrum (Figure 1d) substantiates the Al^{3+} oxidation state in NVO-AVO.[39,40] Figure 1e displays a high-resolution V 2p XPS spectrum, which can be deconvoluted into two doublets corresponding to V^{5+} and V^{4+}. The NVO-AVO composite excites the electron hope between V^{4+} and V^{5+}, improves the electrical conductivity of the electrode material, enhances its ion diffusion kinetics, and stabilizes long-term cycling by interacting with

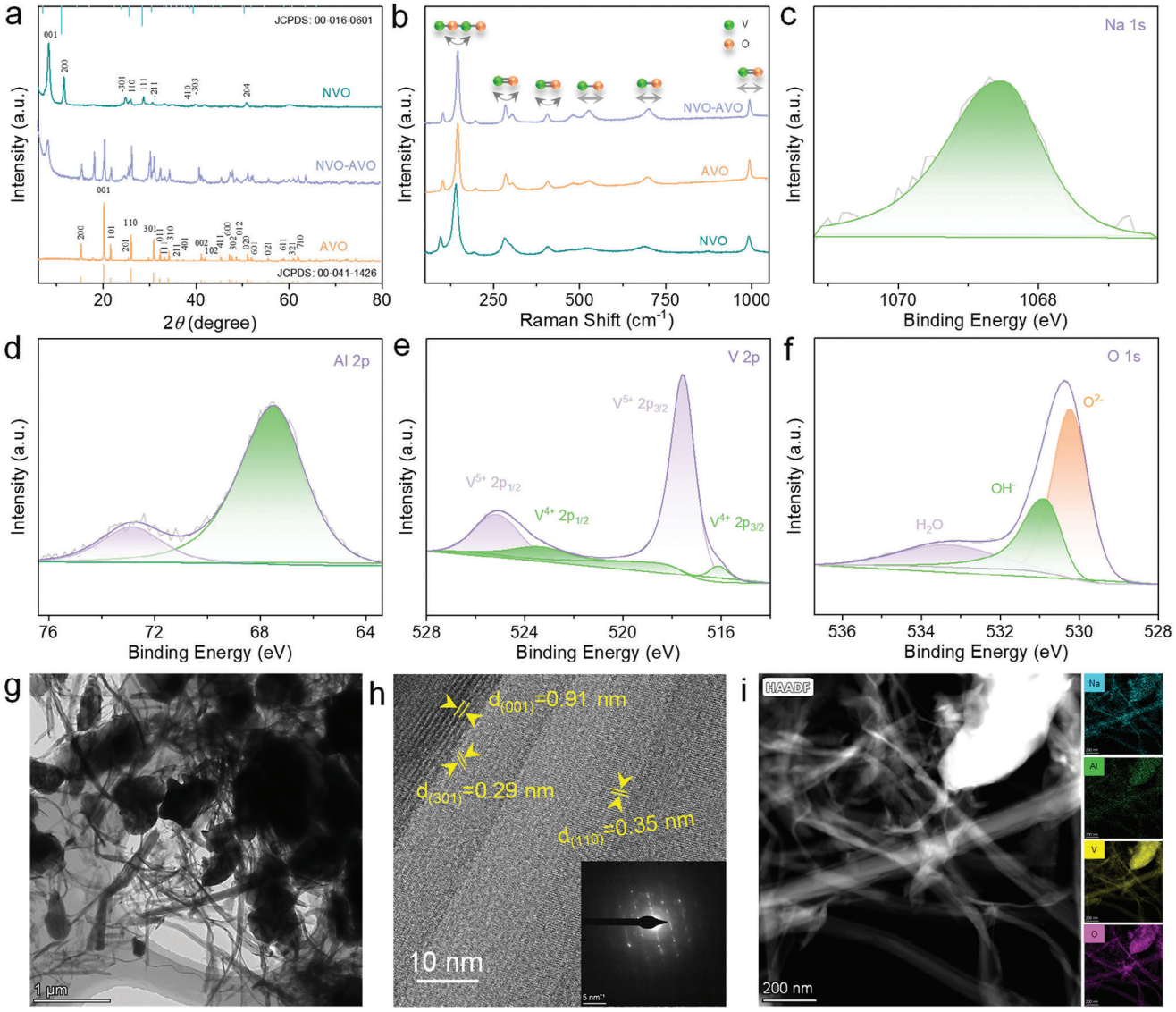

Figure 1. a) Powder XRD patterns and b) Raman spectra of the three active materials. High-resolution XPS spectra of c) Na 1s, d) Al 2p, e) V 2p, and f) O 1s for NVO-AVO. g) TEM image, h) HRTEM image (inset: SAED pattern), i) HAADF image and corresponding Na, Al, V, O element mapping of NVO-AVO.

oxygen in the laminar structure and in the interlayer water. The high-resolution O 1s spectrum of NVO-AVO was fitting to three peaks situated at 530.2 eV (O_1), 530.9 eV (O_2), and 533.5 eV (O_3), respectively, which corresponded to different forms of O^{2-} in V—O, O—H, and H_2O (Figure 1f).

Scanning electron microscope (SEM) and transmission electron microscope (TEM) images show the morphology and particle size of the as-synthesized three active materials. The pristine NVO is in a typical 1D nano ribbons structure (Figures S5a,b, Supporting Information), the AVO is in a nano block structure (Figures S5c,d, Supporting Information) and the NVO-AVO is in nano blocks and nanoribbons bound structure (Figures S5e,f, Supporting Information). The interplanar spacings of NVO are 3.5 and 9.1 Å, corresponding to the (110) and (001) planes, which can be observed in the high-resolution TEM image (HRTEM) (Figure S6, Supporting Information). The interplanar spacing of AVO in Figure S7 (Supporting Information) is 5.8 Å, corresponding to the (200) plane. TEM image further shows that most of the NVO-AVO nano blocks are ≈600 nm in length and ≈500 nm in width, and are evenly surrounded by nanoribbons (Figure 1g). Meanwhile, SEM and TEM images show that most of the NVO nanoribbons have a width of ≈80 nm and a relatively uniform morphology, most of the AVO is surface-smooth nano blocks and most of the nano blocks are less than 1 μm in width. The interplanar spacings are 9.1, 3.5, and 2.9 Å, corresponding to (001), (110), and (301) planes of NVO-AVO (Figure 1h), respectively, which is well matched with the XRD result (Figure 1a). The regular arrangement of discrete spots on the inset Selected Area Electron Diffraction (SAED) pattern of Figure 1h substantiates that NVO-AVO possesses a top-quality single-crystalline nature.

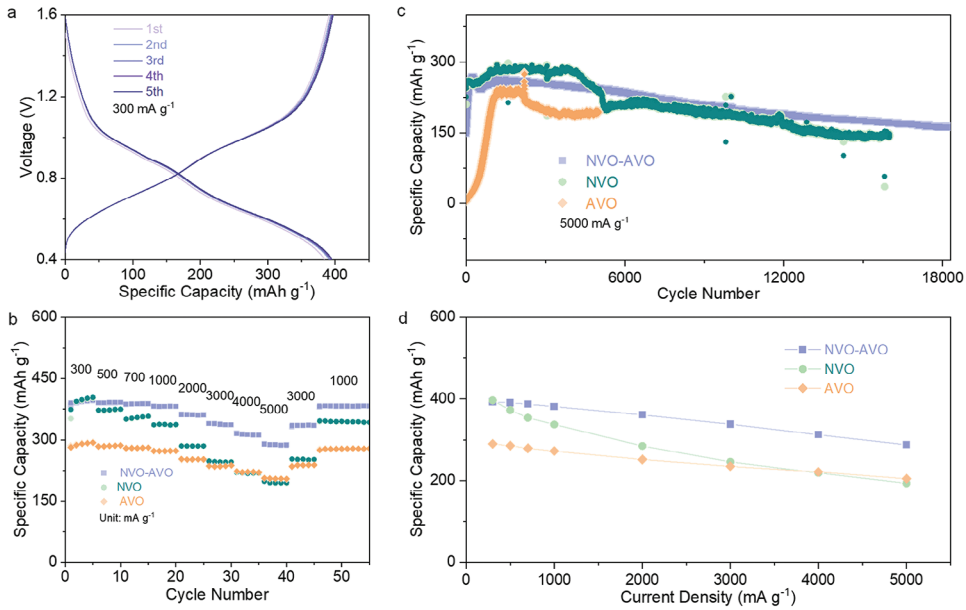

Figure 2. a) Charge–discharge curves of the initial five cycles of NVO-AVO cathode. b) Rate capabilities, c) Long-term cycling stability, d) A comparison of the capacity contribution of the three active materials at different current densities.

HAADF image of elemental mapping corresponding to NVO-AVO (Figure 1i) shows a homogeneous spatial distribution of Na, Al, V, and O elements on nano blocks and nanoribbons, which further demonstrates the successful insertion of Na^+ and Al^{3+} in NVO-AVO. In addition, Figures S6c and S7c (Supporting Information) show that there is also a homogeneous elemental distribution of NVO and AVO.

No work has been reported to discuss and compare this distinct electrochemical characteristic of NVO-AVO. The Zn^{2+} storage properties of NVO-AVO composites have been tested and detailed. Figure S8 (Supporting Information) gives the cyclic voltammeter (CV) curves for the first five cycles of the NVO-AVO electrode at 0.2 mV s^{-1} over the voltage range from 0.4 to 1.6 V. The overlapping CV curves indicate reversible redox reactions, with two pairs of distinct reversible redox peaks at ≈1 V (V^{5+}/V^{4+}) and ≈0.7 V (V^{4+}/V^{3+}), demonstrating that the two-step (de)intercalation of Zn^{2+} is the same as in the other pre-intercalated vanadium oxides.[10,32]

A comparison of the first five-cycle CV curves at 0.2 mV s^{-1} for NVO and AVO is shown in Figure S9 (Supporting Information), with two stable redox peak pairs predominantly for NVO and one stable redox peak pair predominantly for AVO. The charge/discharge profiles of the NVO-AVO composite after pre-cycling at 300 mA g^{-1} are shown in **Figure 2a**. The NVO-AVO delivers an initial discharge capacity of 384.5 mA h g^{-1} and the corresponding charge capacity is 391.0 mA h g^{-1}. The profile shape of the initial discharge was also like the subsequent four cycles, demonstrating highly reversible Zn^{2+} intercalation/deintercalation.

Figure 2b shows the discharge/charge specific capacities of AVO and NVO-AVO at various current densities after pre-cycling. The rate performance of NVO is not pre-cycled. The average discharge-specific capacities of AVO are 288.4, 284.7, 279.8, 272.6, 251.9, 235.9, 221.4, and 204.9 mA h g^{-1} at 300, 500, 700, 1000, 2000, 3000, 4000, and 5000 mA g^{-1}, respectively. The average discharge-specific capacities of NVO-AVO at 300, 500, 700, 1000, 2000, 3000, 4000, and 5000 mA g^{-1} are 391.4, 390.6, 387.5, 381.6, 361.0, 338.2, 313.0, and 287.9 mA h g^{-1}, respectively. The average discharge-specific capacities of NVO at the same current densities are 388.6, 372.7, 353.7, 337.0, 284.8, 246.3, 218.5, and 195.0 mA h g^{-1}. Figure S10 (Supporting Information) presents the corresponding discharge/charge curves for the three active materials at different current densities. At current densities up to 5000 mA g^{-1}, NVO-AVO exhibits a high reversible capacity and retains the clear capacitance gap between NVO and AVO. When the current density increased to 3000 mA g^{-1}, a high reversible capacity (335.0 mA h g^{-1}) was still obtained, indicating the superior rate capability of NVO-AVO. Impressively, after recovering to 1000 mA g^{-1} current density, the reversible capacity easily reverts to 382.0 mA h g^{-1}. Figure S11 (Supporting Information) shows the rate performance of AVO and NVO-AVO without pre-cycled. In the initial stage, with the increase of current density, the discharge capacity of AVO and NVO-AVO also gradually increases, which is consistent with the capacity increase in the initial stage of the following cycle performance.

As presented in Figure S12 (Supporting Information) when the current density is 3000 mA g^{-1}, the specific capacity of NVO-AVO progressively grows from the initial stages, and similar phenomena were seen in other vanadium oxide cathodes for ZIBs.[41,42] This phenomenon may be due to a slow activation process or increased active material utilization.[43] Na and Al coordinate to increase the conductivity of the material, and NVO-AVO offers a high specific capacity of 324.0 mA h g^{-1} with extremely long cycle stability (≈20000 cycles). As a comparison, we also investigated the cycling performance of NVO and AVO. The NVO electrode possesses a capacity of 261.8 mA h g^{-1} in the initial phase, 158.2 mA h g^{-1} after 6000 cycles, and drops sharply for 3000 cycles. Although the initial capacity of AVO (less than

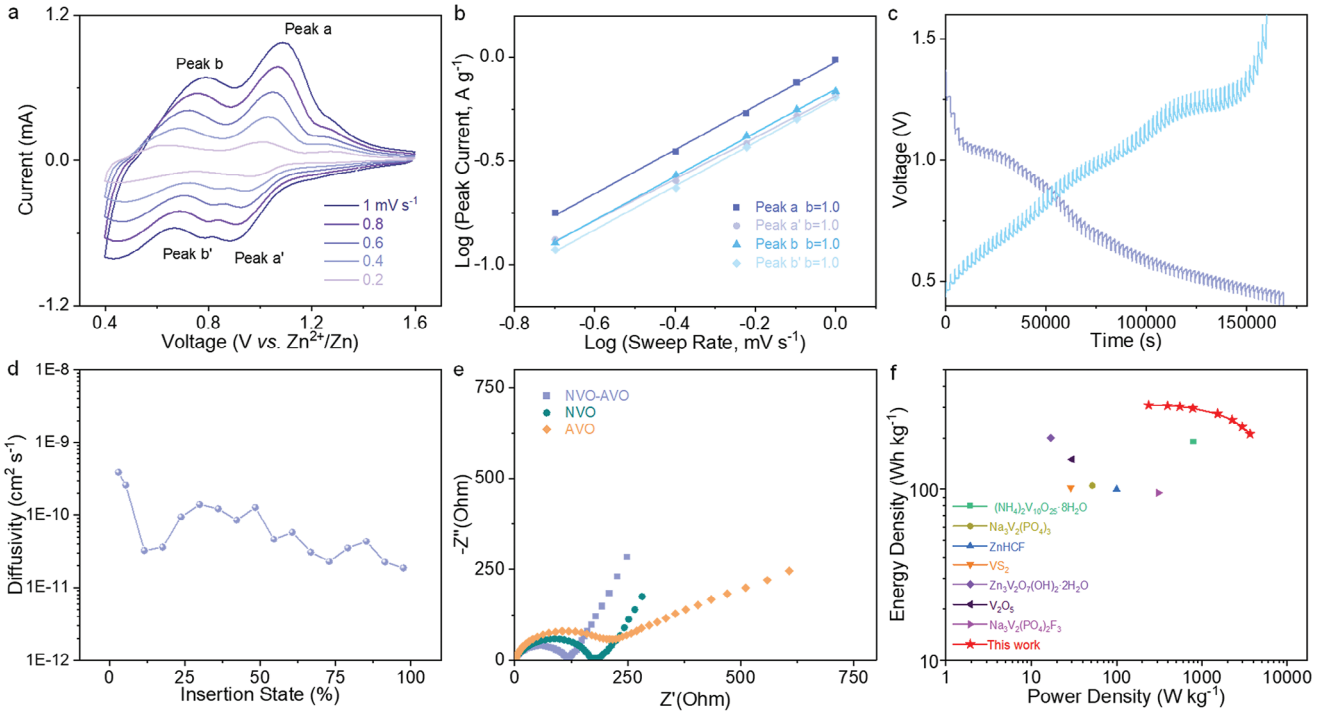

Figure 3. a) CV curves at multiple scan rates b) Relationship between peak currents and scan rates, c) Charge–discharge GITT curves at 50 mA g^{-1}, and d) Zn^{2+} diffusion coefficient for NVO-AVO cathode. e) Nyquist plot and f) Ragone plots of NVO-AVO and other representative cathode materials for AZIBs.

10 mA h g^{-1}) is clearly lower than that of NVO, AVO is much more stable than NVO after the cycling period, and NVO-AVO possesses both high capacity of NVO and stability of AVO. At a high current density of 5000 mA g^{-1} (Figure 2c), the AVO capacity increased rapidly from the initial small value to 235.1 mA h g^{-1} after activation and remained at 195.0 mA h g^{-1} after 5000 cycles. More excitingly, with a capacity of up to 269.5 mA h g^{-1}, NVO-AVO clearly outperforms NVO and AVO, further demonstrating the good long-term cycling stability of NVO-AVO.

The charge/discharge curves for the three materials at 3000 and 5000 mA g^{-1} are presented in Figures S13 and S14 (Supporting Information), respectively. It is noteworthy that even at high current densities the AVO charge/discharge curves are nearly coincident with the 3000th, 4000th, and 5000th cycles, with a Coulombic efficiency in the vicinity of 100%. This shows that the excellent stability of NVO-AVO is mainly attributed to AVO. These results therefore show that aqueous Zn/NVO-AVO batteries hold great promise for meeting commercial applications. The specific capacities of NVO, AVO, and NVO-AVO are summarized in Figure 2d. The fast Zn^{2+} storage and good long-term cycling stability of NVO-AVO are mainly owing to the synergistic effect of NVO and AVO. The ultralong life, ultrahigh capacity, and ultrastability of NVO-AVO exceed most reported AZIBs cathodes (Table S1, Supporting Information). The excellent electrochemical properties indicate that NVO-AVO is a promising material candidate for AZIBs.

CV measurements (**Figure 3a**) were performed at multiple scan rates to investigate the stored charge type of NVO-AVO. The peaks of the CV curves became progressively wider with increasing scan rate and the peak position was slightly shifted. Based on the peak current (i) as a function of the scan rate (v), the capacitance behavior can be determined by the following equation:[44]

$$i = av^b \tag{1}$$

The a and b are adjustable variables. When the value of b is approaching 1.0, the pseudo capacitance dominates the electrochemical reaction processes. When the b value is 0.5, the electrochemical reaction is a diffusion-controlled process. From fitting results in Figure 3b, the b values of the significant redox peak a, a′, b, and b′ are all 1, indicating that the pseudo capacitance plays a major role in the capacity contribution of NVO-AVO. This characteristic favors the fast diffusion kinetics of Zn^{2+}. The CV curves for NVO and AVO and the corresponding log(i)–log(v) curves are shown in Figures S15 and S16 (Supporting Information). Furthermore, it is noteworthy that the capacitive contribution of the NVO-AVO electrode is larger than that of the NVO and AVO electrodes at different sweep rates. As a result, the NVO-AVO electrode shows faster charge transfer kinetics and thus a stronger rate capability.

The Zn^{2+} diffusion coefficient (D_{Zn}) in NVO-AVO was further obtained in Figure 3c using the galvanostatic intermittent titration technique (GITT). Figure 3d shows the calculated D_{Zn} value of NVO-AVO up to 10^{-11}–10^{-10} cm^2 s^{-1}. The excellent electrochemical properties of NVO-AVO are credited to its superior ion diffusion characteristics. The high Zn^{2+} diffusion coefficient is related to the structure of the electrode and the "Block and line combination" structure provides sufficient ion transport channels for rapid ion diffusion. To further reveal the

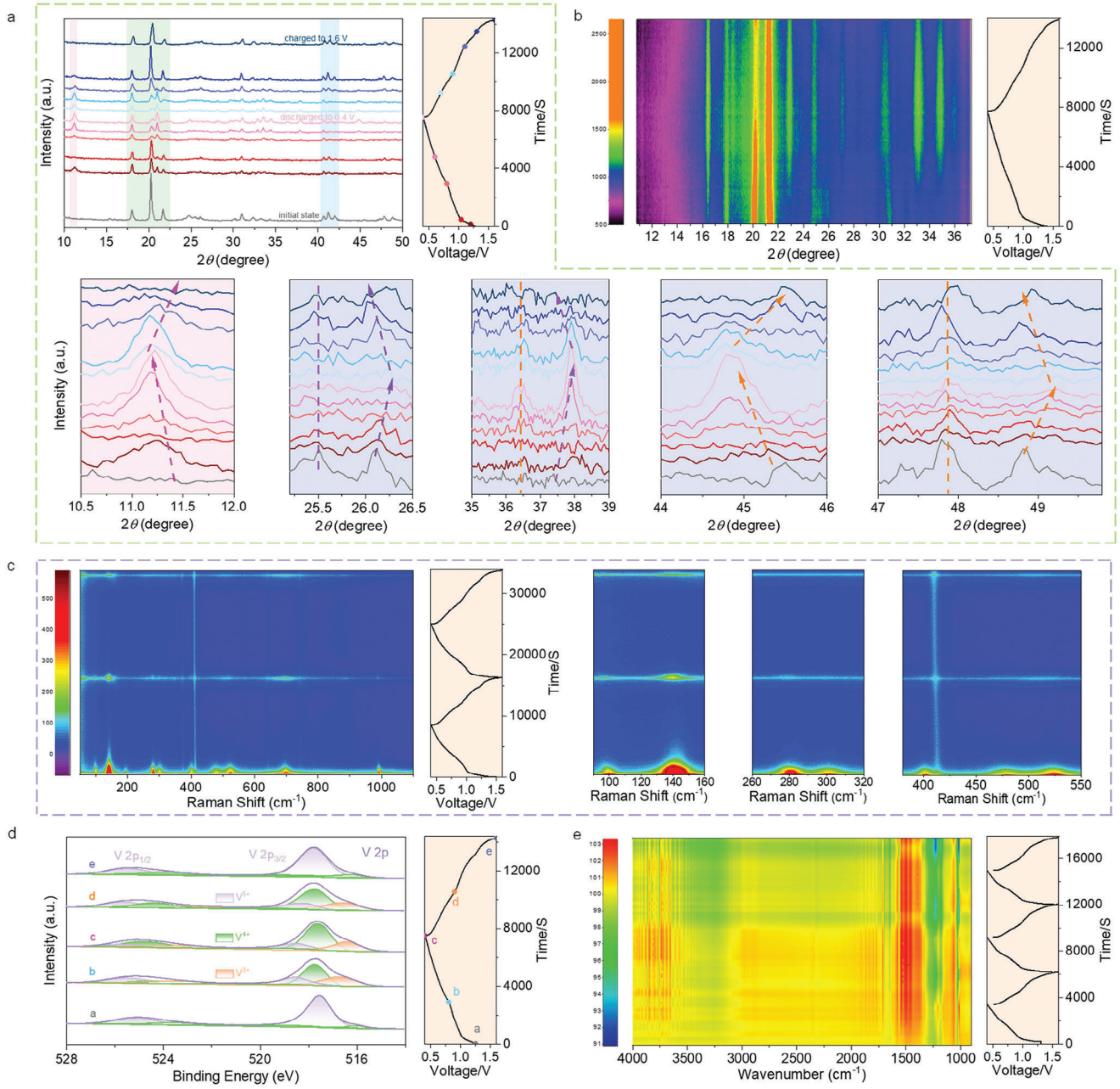

Figure 4. a) Ex situ and b) in situ XRD patterns, c) in situ Raman spectra, ex situ XPS spectra of V 2p d), and in situ FTIR spectra e) of NVO-AVO.

transfer kinetics of Zn^{2+} at the cathode/electrolyte interface, electrochemical impedance spectroscopy (EIS) was carried out. The semicircle diameter of the high-frequency region of the Nyquist plot (Figure 3e) is correlated with the charge-transfer resistance (R_{ct}). NVO-AVO exhibits a much smaller R_{ct} than NVO and AVO, indicating that NVO-AVO possesses a faster surface electron mobility. In addition, NVO-AVO exhibits excellent energy density (310.1 Wh kg^{-1}) as well as impressive power density (3662.6 W kg^{-1}), significantly superior to many reported cathode materials as shown in Figure 3f.[20,41,45–49] Our NVO-AVO is therefore a very promising candidate for the construction of advanced ZIBs.

The excellent performance of NVO-AVO electrodes inspires a deeper understanding of their reaction mechanisms. In order to probe the structural evolution of NVO-AVO, ex situ XRD patterns were analyzed in selected states (**Figure** 4a). The peaks (001) at 20.3°, (101) at 21.7°, (002) at 41.3°, and (102) at 42.1° become progressively weaker when discharging and stronger when charging. During discharge, new peaks were observed near 21.0° and 36.5°, corresponding to peaks (011) and (021), respectively, indicating the production of zinc vanadate hydroxide ($Zn_3(OH)_2V_2O_7{\cdot}2H_2O$, JCPDS: 00-050-0570), which became progressively stronger as discharge proceeded and gradually disappeared with charging.[50,51] The magnified peak clearly shows that

the (200) peak at 11.5° becomes stronger and shifts to a lower angle as the Zn^{2+} insertion process and weaker and shifts to a higher angle as the deintercalation of Zn^{2+}. The (201) peak at 25.5° becomes weaker and weaker as it is discharged and more robust as charged. The (110) peak at 26.2° and the (012) peak at 48.9° become progressively weaker and shift to the right as the discharge progresses, and the peak intensity becomes progressively more robust and shifts to the left as the charge progresses. The peak (401) at 37.6° becomes progressively stronger and shifted to the right when discharging, and progressively weaker and shifted to the left when charging. The peak (411) at 45.56° gradually becomes weaker and then stronger when discharging and moves to lower 2θ values, after charging it reverses back to its original value also becoming weaker and then stronger. The peak (302) at 47.9° becomes progressively weaker and shifted to the left when discharging, and progressively stronger and shifted to the right when charging. After charging, the peaks of the above changes all returned to their original positions as Zn^{2+} was extracted, indicating that the NVO-AVO electrode possesses a reversible structure during Zn^{2+} intercalation/deintercalation.

The in situ XRD patterns in Figure 4b show more pronounced that the peak intensity of the characteristic NVO-AVO peak changes with the (de)intercalation of Zn^{2+}, but without significant shift, indicating that it exhibits good structural stability during cycling, which is conducive to its cycling performance. Furthermore, in situ Raman spectroscopy provided further insight into the reaction mechanism of the NVO-AVO electrode over the electrochemical process (Figure 4c). As the first discharge proceeds, the peaks at 100, 141.1, and 281.3 cm^{-1} are slightly shifted to the left and gradually disappear (as can be clearly seen in the enlarged in situ Raman spectra), with the intensity gradually becoming stronger on charging. These peaks fade in intensity at fully discharged voltages and recover in the fully charged state, associated with (de)insertion of Zn^{2+}. At the same time, the peaks at 301.3, 401.8, 478.3, and 524.1 cm^{-1} become weaker during discharge and progressively stronger during charging. The appearance of the peak at 413 cm^{-1} throughout the discharge and charging process is due to the sapphire substrate.[52] The peaks at 700 and 993.3 cm^{-1} are shifted to the left and fade away when discharging and become progressively stronger when charging (as can be clearly seen in Figure S17, Supporting Information). Correspondingly, the ex situ Raman results during charging and discharging are depicted in Figure S18 (Supporting Information), and the results are in high agreement with the in situ Raman tests. The periodic disappearance or appearance of these characteristic Raman peaks demonstrates that the electrochemical reaction is fully reversible, suggesting good reversibility of the Zn^{2+} intercalation/deintercalation from the NVO-AVO electrode.

To explore the evolution in the chemical valence of the NVO-AVO electrode, ex situ XPS tests were carried out on different states of the electrode (Figure 4d). In the pristine state, the V 2p XPS region with the majority of V^{5+} peaks, accompanied by a small fraction of V^{4+} peaks. During discharge, the V^{4+} component gradually increases, while the V^{5+} component obviously decreases and the V^{3+} peak appears. When charged to 1.6 V, the V^{3+} component disappears, the V^{5+} peak dominates and the V^{4+} component decreases, V 2p spectrum almost returns to its initial state, indicating a highly reversible redox reaction of V species occurs. Figure S19 (Supporting Information) shows the XPS spectra of Zn 2p in different states, with no detectable Zn signal in the pristine state. In the fully discharged state, two strong and sharp Zn signal peaks appear at 1019.6 and 1042.6 eV, indicating the insertion of Zn^{2+} in NVO-AVO. When charged to 1.6 V, the Zn 2p peak diminishes significantly, showing that most of the Zn^{2+} is taken out from the NVO-AVO. These results are further supported by the analysis of elemental mapping images of the different states (Figures S20–22, Supporting Information).

Figure 4e shows the in situ FTIR spectra of the NVO-AVO electrode in different electrochemical states. The V═O peak intensity at 1030.6 cm^{-1} becomes progressively weaker with charging and stronger with discharging. The peak at 3483.7 cm^{-1} represents the O—H stretching vibration, which becomes weaker during charging and stronger during discharging and remains consistent with the bending vibration O—H change of 1641.9 cm^{-1}. All peaks are not significantly shifted, suggesting that the molecular structure stays stable during the electrochemical process, which is beneficial for the stability of the long-cycle performance. In situ EIS study was performed further to explore the electrochemical behavior of the NVO-AVO electrode, as shown in Figures S23 and S24 (Supporting Information). The R_{ct} of the NVO-AVO was 109.2 Ω in the initial state, dropping to 18.5 Ω when discharged to 0.4 V and 49.1 Ω when fully charged. During the first discharge cycle, R_{ct} decreases significantly and rapidly. During the charging phase, R_{ct} decreases slowly, probably due to the activation of the material.

The remarkable energy and power densities of NVO-AVO facilitate their use in flexible energy storage devices. Accordingly, a soft packaged NVO-AVO//Zn cell was assembled by sandwiching the separator and electrolyte between the NVO-AVO positive electrode and the zinc foil negative electrode (**Figure 5a**). Figure 5b displays the cycling performance of the NVO-AVO//Zn soft pack battery at 400 mA g^{-1}, with a discharge capacity of 131.8 mA h g^{-1} on the first cycle and still 143.7 mA h g^{-1} after 70 cycles. Figure 5c shows the charge/discharge curve of the soft pack battery NVO-AVO//Zn at 400 mA g^{-1}. Additionally, the Coulombic efficiency is ≈100% throughout the cycle, indicating that the soft-packaged battery NVO-AVO//Zn has good electrochemical reversibility during repeated charging and discharging. To further indicate the viability of a soft-packaged NVO-AVO//Zn battery as a flexible energy storage device, two soft-packaged cells were connected in series and easily illuminated by a "WUT" shaped logo light containing 55 LEDs (Figure 5d). The soft pack can still light up the LEDs no matter how much it is bent (Figure 5e) or even cut open (Figure 5f), and the voltage does not change significantly (Figure 5g–i). This shows that soft-pack NVO-AVO//Zn cells are promising for practical applications in flexible energy storage devices.

3. Conclusion

In summary, we used low-cost V_2O_5 as a feedstock to develop a low-cost, simple, and efficient strategy for designing a novel NVO-AVO composite for the first time that combines monoclinic and orthogonal materials. Based on experimental results, we find that the unique structure of the NVO-AVO composite makes it possible to take full advantage of the synergy between the high specific capacitance of NVO and the excellent cycling performance of AVO. NVO-AVO exhibits a higher

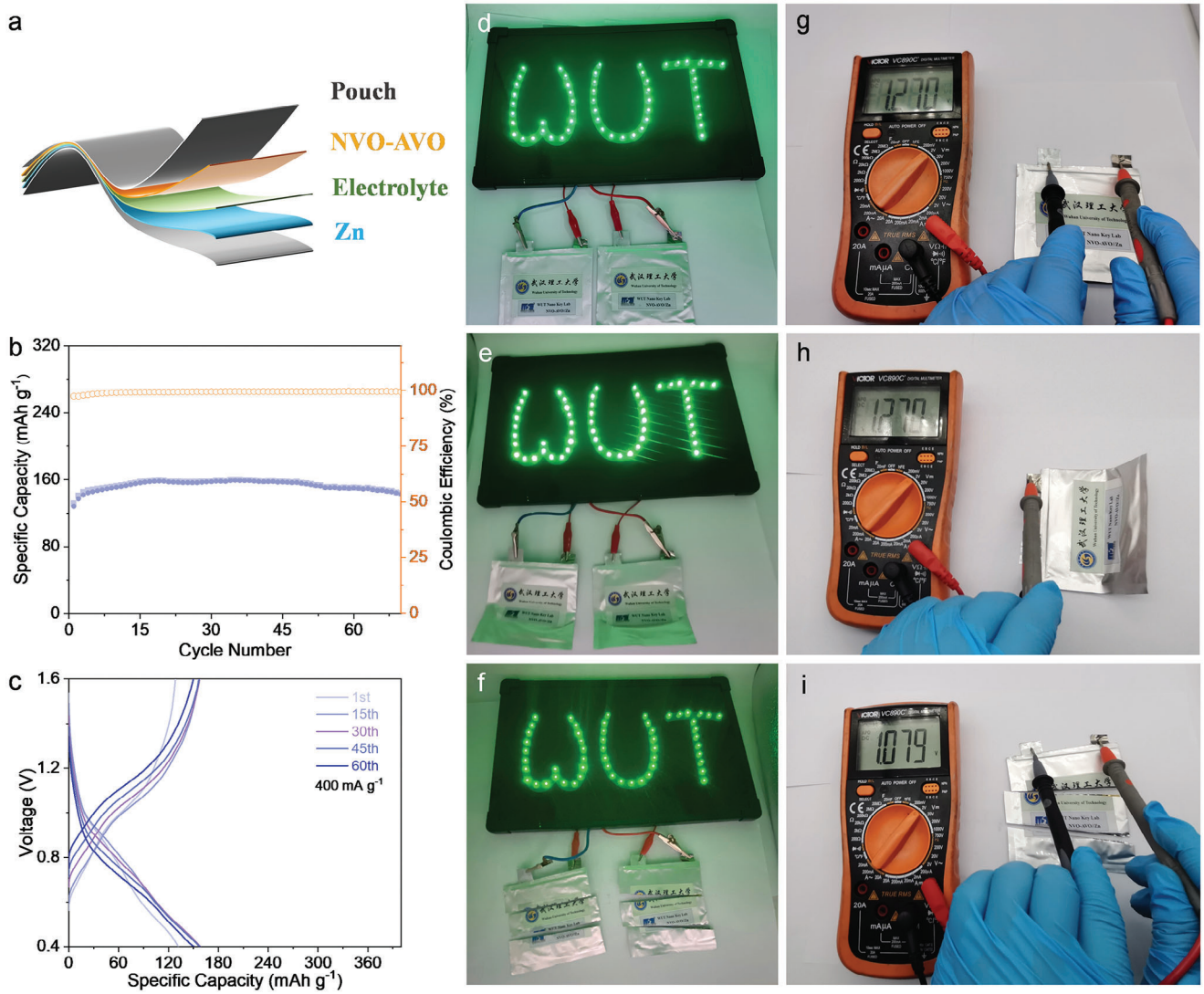

Figure 5. a) Schematic of the structure of the flexible NVO-AVO//Zn soft pack battery. b) Cycling performance. c) Typical charge and discharge curves. d–f) Two soft pack cells in series illuminate the led signs for normal, 90° bend, and cut states. g–i) Voltage of the soft pack in normal, 90° bending and cutting conditions.

electronic conductivity and electronic structure, which improves the reaction kinetics and lowers the polarization, resulting in a greatly improved battery performance. The electrochemical measurement results indicate that the synthesized NVO-AVO composite as an AZIB cathode shows an enhanced capacity of 392.5 mA h g^{-1} at 300 mA g^{-1}, higher than the 289.8 mA h g^{-1} of AVO. The NVO-AVO composite exhibits good cycling stability, with a capacity of 160.6 mA h g^{-1} after 18 300 cycles at 5000 mA g^{-1}, while the NVO delivers a capacity of 142.1 mA h g^{-1} after 16 000 cycles. The NVO-AVO electrode also exhibits high energy density and power density. Therefore, NVO-AVO demonstrates great application value as a cathode material for next-generation energy storage systems. We believe that the promising electrochemical results obtained in this work, together with insights into the mechanism of Zn storage, bring low-cost room temperature AZIBs closer to becoming sustainable large-scale energy storage systems.

4. Experimental Section

Fabrication of NVO-AVO: Briefly, 5.6 g V_2O_5, 2.3 g Na_2SO_4, and 3.1 g $Al_2(SO_4)_3{\cdot}18H_2O$ were added to 66 mL of deionized (DI) water under vigorous stirring at 25 °C and under the same conditions the pH was adjusted to 2.8 with hydrochloric acid. The mixture was shifted to a 100 mL autoclave and kept at 180 °C for 72 h. The orange precipitate (NVO-AVO) was then thoroughly washed with DI water and ethanol and finally allowed to dry under vacuum at 60 °C for 12 h. As a comparison, the synthesis process was slightly modified (without the addition of aluminum and sodium sources) to give aluminum-free vanadium oxide (NVO) and sodium-free vanadium oxide (AVO) as comparative samples.

Supporting Information

Supporting Information is available from the Wiley Online Library or from the author.

Acknowledgements

L. X. and X. Z. contributed equally to this work. This work was supported by the Natural Science Foundation of Hubei Province (2022CFA087, 2023AFB999), the National Natural Science Foundation of China (52302304), and the Guangdong Basic and Applied Basic Research Foundation (2021A1515110059). Support from the China Scholarship Council (CSC, 202106950026).

Conflict of Interest

The authors declare no conflict of interest.

Data Availability Statement

The data that support the findings of this study are available from the corresponding author upon reasonable request.

Keywords

aqueous zinc ion batteries, long-term cycling stability, synergistic effect, vanadium-based composites

Received: October 16, 2023
Revised: November 18, 2023
Published online: December 22, 2023

[1] H. Liu, Q. Ye, D. Lei, Z. Hou, W. Hua, Y. Huyan, N. Li, C. Wei, F. Kang, J.-G. Wang, *Energy Environ. Sci.* **2023**, *16*, 1610.
[2] X. Gao, Y. H. Dai, C. Y. Zhang, Y. X. Zhang, W. Zong, W. Zhang, R. W. Chen, J. X. Zhu, X. Y. Hu, M. Y. Wang, R. Z. Chen, Z. J. Du, F. Guo, H. B. Dong, Y. Y. Liu, H. Z. He, S. Y. Zhao, F. J. Zhao, J. W. Li, I. P. Parkin, C. J. Carmalt, G. J. He, *Angew. Chem., Int. Ed.* **2023**, *62*, 2300608.
[3] Y. Li, X. Peng, X. Li, H. Duan, S. Xie, L. Dong, F. Kang, *Adv. Mater.* **2023**, *35*, 2300019.
[4] B. Jin, Y. Liu, J. Cui, S. Zhang, Y. Wu, A. Xu, M. Xu, M. Shao, *Adv. Funct. Mater.* **2023**, *33*, 2301909.
[5] C. Liu, M. Li, J. Meng, P. Hei, J. Wang, Y. Song, X.-X. Liu, *Adv. Funct. Mater.* **2023**, 2310437, https://doi.org/10.1002/adfm.202310437.
[6] R. Zhao, J. Yang, X. Han, Y. Wang, Q. Ni, Z. Hu, C. Wu, Y. Bai, *Adv. Energy Mater.* **2023**, *13*, 2203542.
[7] S. Zhao, Y. Zhang, J. Li, L. Qi, Y. Tang, J. Zhu, J. Zhi, F. Huang, *Adv. Mater.* **2023**, *35*, 2300195.
[8] Y. Qin, H. Li, C. Han, F. Mo, X. Wang, *Adv. Mater.* **2022**, *34*, 2207118.
[9] B. Niu, Z. Li, D. Luo, X. Ma, Q. Yang, Y.-E. Liu, X. Yu, X. He, Y. Qiao, X. Wang, *Energy Environ. Sci.* **2023**, *16*, 1662.
[10] L. Xing, C. Zhang, M. Li, P. Hu, X. Zhang, Y. Dai, X. Pan, W. Sun, S. Li, J. Xue, Q. An, L. Mai, *Energy Stor. Mater.* **2022**, *52*, 291.
[11] Y. Zong, H. He, Y. Wang, M. Wu, X. Ren, Z. Bai, N. Wang, X. Ning, S. X. Dou, *Adv. Energy Mater.* **2023**, *13*, 2300403.
[12] Y. Chen, D. Ma, S. Shen, P. Deng, Z. Zhao, M. Yang, Y. Wang, H. Mi, P. Zhang, *Energy Stor. Mater.* **2023**, *56*, 600.
[13] G. Li, L. Sun, S. Zhang, C. Zhang, H. Jin, K. Davey, G. Liang, S. Liu, J. Mao, Z. Guo, *Adv. Funct. Mater.* **2023**, 2301291, https://doi.org/10.1002/adfm.202301291.
[14] J. Yang, R. Zhao, Y. Wang, Z. Hu, Y. Wang, A. Zhang, C. Wu, Y. Bai, *Adv. Funct. Mater.* **2023**, 2213510.
[15] Z. Gong, Z. Li, P. Wang, K. Jiang, Z. Bai, K. Zhu, J. Yan, K. Ye, G. Wang, D. Cao, G. Chen, *Energy Mater. Adv.* **2023**, *4*, 0035.
[16] J. J. Yang, R. Zhao, Y. H. Wang, Y. Bai, C. Wu, *Energy Mater. Adv.* **2022**, *2022*, 9809626.
[17] Z. Sang, J. Liu, X. Zhang, L. Yin, F. Hou, J. Liang, *ACS Nano* **2023**, *17*, 3077.
[18] L. E. Blanc, D. Kundu, L. F. Nazar, *Joule* **2020**, *4*, 771.
[19] Y. Xu, G. Zhang, J. Liu, J. Zhang, X. Wang, X. Pu, J. Wang, C. Yan, Y. Cao, H. Yang, W. Li, X. Li, *Energy Environ. Mater.* **2023**, e12575, https://doi.org/10.1002/eem2.12575.
[20] L. Zhang, L. Chen, X. Zhou, Z. Liu, *Adv. Energy Mater.* **2015**, *5*, 1400930.
[21] Y. Zhang, F. Wan, S. Huang, S. Wang, Z. Niu, J. Chen, *Nat. Commun.* **2020**, *11*, 2199.
[22] W. Li, C. Han, Q. Gu, S.-L. Chou, J.-Z. Wang, H.-K. Liu, S.-X. Dou, *Adv. Energy Mater.* **2020**, *10*, 2001852.
[23] S. Liu, H. Zhu, B. Zhang, G. Li, H. Zhu, Y. Ren, H. Geng, Y. Yang, Q. Liu, C. C. Li, *Adv. Mater.* **2020**, *32*, 2001113.
[24] Y. Lu, T. Zhu, W. Van Den Bergh, M. Stefik, K. Huang, *Angew. Chem., Int. Ed.* **2020**, *59*, 17004.
[25] H. Jiang, Y. Zhang, M. Waqar, J. Yang, Y. Liu, J. Sun, Z. Feng, J. Sun, Z. Pan, C. Meng, J. Wang, *Adv. Funct. Mater.* **2022**, *33*, 2213127.
[26] Y. Zhu, M. Yang, Q. Huang, D. Wang, R. Yu, J. Wang, Z. Zheng, D. Wang, *Adv. Mater.* **2020**, *32*, 1906205.
[27] X. Wang, Y. Li, S. Wang, F. Zhou, P. Das, C. Sun, S. Zheng, Z.-S. Wu, *Adv. Energy Mater.* **2020**, *10*, 2000081.
[28] Y. Yang, Y. Tang, G. Fang, L. Shan, J. Guo, W. Zhang, C. Wang, L. Wang, J. Zhou, S. Liang, *Energy Environ. Sci.* **2018**, *11*, 3157.
[29] X. Tang, P. Wang, M. Bai, Z. Wang, H. Wang, M. Zhang, Y. Ma, *Adv. Sci.* **2021**, *8*, 2102053.
[30] P. He, G. Zhang, X. Liao, M. Yan, X. Xu, Q. An, J. Liu, L. Mai, *Adv. Energy Mater.* **2018**, *8*, 1702463.
[31] Y. Yang, Y. Tang, S. Liang, Z. Wu, G. Fang, X. Cao, C. Wang, T. Lin, A. Pan, J. Zhou, *Nano Energy* **2019**, *61*, 617.
[32] M. Yan, P. He, Y. Chen, S. Wang, Q. Wei, K. Zhao, X. Xu, Q. An, Y. Shuang, Y. Shao, K. T. Mueller, L. Mai, J. Liu, J. Yang, *Adv. Mater.* **2018**, *30*, 1703725.
[33] S. Li, X. Xu, K. Wang, W. Chen, X. Lu, Z. Song, J.-Y. Hwang, J. Kim, Y. Bai, Y. Liu, S. Xiong, *ACS Energy Lett.* **2022**, *7*, 3770.
[34] V. Soundharrajan, B. Sambandam, S. Kim, M. H. Alfaruqi, D. Y. Putro, J. Jo, S. Kim, V. Mathew, Y.-K. Sun, J. Kim, *Nano Lett.* **2018**, *18*, 2402.
[35] Q. Pang, W. He, X. Yu, S. Yang, H. Zhao, Y. Fu, M. Xing, Y. Tian, X. Luo, Y. Wei, *Appl. Surf. Sci.* **2021**, *538*, 148043.
[36] J. Li, K. Mccoll, X. Lu, S. Sathasivam, H. Dong, L. Kang, Z. Li, S. Zhao, A. G. Kafizas, R. Wang, D. J. L. Brett, P. R. Shearing, F. Corà, G. He, C. J. Carmalt, I. P. Parkin, *Adv. Energy Mater.* **2020**, *10*, 2000058.
[37] X. Zhu, Z. Cao, X.-L. Li, L. Pei, J. Jones, Y.-N. Zhou, P. Dong, L. Wang, M. Ye, J. Shen, *Energy Stor. Mater.* **2022**, *45*, 568.
[38] D. Chen, H. Chen, C.-F. Du, L. Liu, H. Geng, H. Yu, X. Rui, *J. Mater. Chem. A* **2022**, *10*, 5479.
[39] S. Tonda, S. Kumar, M. Bhardwaj, P. Yadav, S. Ogale, *ACS Appl. Mater. Interfaces* **2018**, *10*, 2667.
[40] X. Xu, S. Shi, Y. Tang, G. Wang, M. Zhou, G. Zhao, X. Zhou, S. Lin, F. Meng, *Adv. Sci.* **2021**, *8*, 2002658.
[41] F. Wan, L. Zhang, X. Dai, X. Wang, Z. Niu, J. Chen, *Nat. Commun.* **2018**, *9*, 1656.
[42] Q. Zong, Q. Wang, C. Liu, D. Tao, J. Wang, J. Zhang, H. Du, J. Chen, Q. Zhang, G. Cao, *ACS Nano* **2022**, *16*, 4588.
[43] W. Yang, X. Du, J. Zhao, Z. Chen, J. Li, J. Xie, Y. Zhang, Z. Cui, Q. Kong, Z. Zhao, C. Wang, Q. Zhang, G. Cui, *Joule* **2020**, *4*, 1557.
[44] T. Brezesinski, J. Wang, S. H. Tolbert, B. Dunn, *Nat. Mater.* **2010**, *9*, 146.
[45] H. Jiang, Y. Zhang, Y. Liu, J. Yang, L. Xu, P. Wang, Z. Gao, J. Zheng, C. Meng, Z. Pan, *J. Mater. Chem. A* **2020**, *8*, 15130.
[46] P. He, M. Yan, G. Zhang, R. Sun, L. Chen, Q. An, L. Mai, *Adv. Energy Mater.* **2017**, *7*, 1601920.

[47] C. Xia, J. Guo, Y. Lei, H. Liang, C. Zhao, H. N. Alshareef, *Adv. Mater.* **2018**, *30*, 1705580.
[48] P. Hu, M. Yan, T. Zhu, X. Wang, X. Wei, J. Li, L. Zhou, Z. Li, L. Chen, L. Mai, *ACS Appl. Mater. Interfaces* **2017**, *9*, 42717.
[49] W. Li, K. Wang, S. Cheng, K. Jiang, *Energy Stor. Mater.* **2018**, *15*, 14.
[50] X. Wang, Y. Wang, Y. Jiang, X. Li, Y. Liu, H. Xiao, Y. Ma, Y.-Y. Huang, G. Yuan, *Adv. Funct. Mater.* **2021**, *31*, 2103210.
[51] H. Li, Z. Liu, G. Liang, Y. Huang, Y. Huang, M. Zhu, Z. Pei, Q. Xue, Z. Tang, Y. Wang, B. Li, C. Zhi, *ACS Nano* **2018**, *12*, 3140.
[52] L. Xing, K. A. Owusu, X. Liu, J. Meng, K. Wang, Q. An, L. Mai, *Nano Energy* **2021**, *79*, 105384.